

Phosphorous and Nitrogen Dual-Doped Carbon as a Highly Efficient Electrocatalyst for Sodium-Oxygen Batteries

Haipeng Guo

Australian Institute for Innovative Materials, Institute for Superconducting and Electronic Materials, University of Wollongong, Innovation Campus, Squires Way, North Wollongong, NSW 2522, Australia

Zhi Zheng

University of Wollongong

Chaozhu Shu

University of Wollongong

Zhe Hu

Australian Institute for Innovative Materials, Institute for Superconducting and Electronic Materials, University of Wollongong, Innovation Campus, Squires Way, North Wollongong, NSW 2522, Australia

Florian Gebert

University of Wollongong

Qinfen Gu

Australian Nuclear Science and Technology Organisation <https://orcid.org/0000-0001-9209-4208>

Konstantin Konstantinov

University of Wollongong <https://orcid.org/0000-0003-4919-6385>

Shulei Chou (✉ shulei@uow.edu.au)

Australian Institute for Innovative Materials, Institute for Superconducting and Electronic Materials, University of Wollongong, Innovation Campus, Squires Way, North Wollongong, NSW 2522, Australia.

<https://orcid.org/0000-0003-1155-6082>

Huakun Liu

University of Wollongong <https://orcid.org/0000-0002-0253-647X>

Jiazhao Wang

University of Wollongong

Article

Keywords: sodium-oxygen batteries, PNDC, applications, electrocatalysts, discharge products

Posted Date: September 16th, 2020

DOI: <https://doi.org/10.21203/rs.3.rs-74647/v1>

License:  This work is licensed under a Creative Commons Attribution 4.0 International License.

[Read Full License](#)

Abstract

Sodium-oxygen batteries have been regarded as promising energy storage devices due to their low overpotential and high energy density. Its applications, however, still face formidable challenges due to the lack of understanding about the influence of electrocatalysts on discharge products. Here, a phosphorous and nitrogen dual-doped carbon (PNDC) based cathode is synthesized to increase the electrocatalytic activity and to stabilize the NaO₂ nanoparticle discharge products, leading to enhanced cycling stability when compared with the nitrogen-doped carbon (NDC). The PNDC air cathode exhibits a quite low overpotential (0.36 V) and long cycling stability for 120 cycles. The reversible formation/decomposition and stabilize ability of NaO₂ discharge products are clearly proven by in-situ synchrotron X-ray diffraction and ex-situ X-ray diffraction. Based on the density functional theory calculation, the PNDC has much stronger adsorption energy (-2.85 eV) for NaO₂ than that of NDC (-1.80 eV), which could efficiently stabilize the NaO₂ discharge products.

Introduction

Lithium-oxygen batteries have received great attention during the past several years because of their high energy density and power density.^{1, 2, 3} Unfortunately, there are still many problems impede its practical application, such as high overpotential and poor cycling stability.^{4, 5, 6, 7, 8, 9} The main reason for these problems could be attributed to the formation of an extremely unstable superoxide intermediate (O₂⁻), which could not be stabilized by small Li⁺ ions due to the mismatch according to the hard and soft acid base (HSAB) theory and can react with non-aqueous electrolytes or carbon-based air cathodes.^{10, 11, 12} By contrast, as a soft Lewis acid compared with Li⁺, Na⁺ could effectively stabilize the soft Lewis base O₂⁻ ions. Therefore, sodium-oxygen batteries (Na-O₂ batteries) have been considered as a more promising system due to the formation of more stable discharge product, sodium superoxide (NaO₂), leading to low overpotential and high reversibility.^{13, 14, 15, 16, 17, 18, 19, 20, 21, 22, 23, 24} However, other distinct sodium oxides, such as sodium peroxide (Na₂O₂) and sodium peroxide dihydrate (Na₂O₂·2H₂O), also have been reported as main discharge products of Na-O₂ batteries, which could significantly affect the electrochemical performance in such aspects as overpotential, energy efficiency, and cycling stability.^{25, 26, 27, 28, 29, 30, 31, 32, 33, 34, 35} In addition, even with NaO₂ as the primary discharge product, it also could be transformed into Na₂O₂·2H₂O with spontaneous dissolution and ionization.^{36, 37, 38, 39} Therefore, it is important to achieve an in-depth understanding of the influence of electrocatalysts on the composition of discharge products and to prevent the transformation of NaO₂, which is a prerequisite for developing efficient catalysts with high-performance and long-life cycling stability.^{40, 41, 42} Owing to the tunability of their structure and surface properties, carbonaceous based materials have been extensively studied as efficient catalysts for various catalytic reactions.^{43, 44, 45, 46, 47} The catalytic performance of carbon based materials could also be improved through doping with different elements, such as phosphorus, sulfur, or boron.^{48, 49, 50, 51, 52,}

^{53, 54} Thus, it is considered that carbonaceous materials with tunable structure and surface properties are one of the most promising types of catalytic materials for Na-O₂ chemistry.

In this work, a heteroatom-doped carbon-based cathode has been designed, and the influence of carbon catalysts doped with different heteroatoms has been studied with respect to the electrocatalytic activities, composition of discharge products, and electrocatalytic performance of Na-O₂ batteries. Carbon materials with different doping, namely, the phosphorus and nitrogen dual-doped carbon (PNDC) and nitrogen-doped carbon (NDC), were fabricated and studied as electrocatalysts for the Na-O₂ batteries. When the two different doped carbon materials were evaluated as air cathodes for the Na-O₂ batteries, different electrocatalytic performance were observed due to their different electrocatalytic activity and distinct stabilize abilities to the discharge products. Thanks to the strong adsorption energy, the PNDC could prevent the dissolution and ionization of NaO₂ nanoparticle discharge product to Na₂O₂·2H₂O. Therefore, PNDC based Na-O₂ batteries demonstrate a quite low overpotential of about 0.36 V and excellent cycling stability for 120 cycles.

Results

Materials characterizations

Polypyrrole (PPy) hollow nanotubes were first synthesized through the polymerization of pyrrole monomer with methyl orange as template. Afterwards, PNDC was fabricated by annealing PPy at 300 °C in argon atmosphere with NaH₂PO₂ as the P precursor, as illustrated in Fig. 1a. NDC was also prepared through directly annealing PPy at 300 °C in argon atmosphere. The structure and morphology of the samples were studied by scanning electron microscopy (SEM) and scanning transmission electron microscopy (STEM), as shown in Fig. 1b-h, Supplementary Figs. 1 and 2. The as prepared polypyrrole has a tubular structure with the tube diameter around 400 nm and length up to 10 μm (Supplementary Fig. 1). After the doping process, the tubal structures are well preserved for both PNDC and NDC (Fig. 1b-d and Supplementary Fig. 2). Then energy dispersive X-ray spectroscopy (EDS) mapping was conducted to study the element distributions within the tubal carbon (Fig. 1 and Supplementary Figs. 2 and 3). As shown in Fig. 1e and f, the doping elements (P and N) are homogeneously distributed in the carbon tubal structures of the PNDC. In the NDC, nitrogen is also evenly distributed throughout the whole tubal structure (Supplementary Fig. 2). In addition, the high resolution TEM images reveal the porous structure of PNDC, which could supply plentiful active sites and adequate space for gas diffusion and electrolyte impregnation as well as discharge products accommodation. (Supplementary Fig. 4).

Further information on the structure and surface chemical status of the samples were obtained from Raman spectroscopy and X-ray photoelectron spectroscopy (XPS) (Fig. 1g-h and Supplementary Fig. 5–7). The surface chemistries of PNDC and NDC are different due to their differences in element doping. As shown in Supplementary Fig. 5a, the XPS survey scan of PNDC demonstrates the presence of P, N, and C without any impurities on the surface, which is consistent with the EDS results. The P and N elemental content is 2.36 atom % and 8.26 atom %, respectively. NDC also has similar N content of about 8.50 atom

% (Supplementary Fig. 6a). The high-resolution C 1s spectra of PNDC (Supplementary Fig. 5b) and NDC (Supplementary Fig. 6b) can be deconvoluted into three component peaks, corresponding to C-C/C = C, C-N, and C = O. The only difference is that the C = O peak of PNDC (288.6 eV) is shifted to higher binding energy compared with that of NDC (287.9 eV), which may be caused by the doping with P atoms. On the other hand, the high-resolution N1s spectra of PNDC and NDC show three nitrogen species (pyridinic-N, pyrrolic-N, and graphitic-N), implying that part of the pyrrolic-N atoms within the polypyrrole rings are transformed to pyridinic-N and graphitic-N (Fig. 1h and Supplementary Fig. 6c). Compared with NDC, the graphitic-N peak of PNDC is shifted to lower binding energy (from 402.4 to 401.7 eV). In addition, when compared with NDC, the content of graphitic-N for PNDC decreased from 17.0% to 10.1%, while the content of pyrrolic-N increased from 64.9% to 67.3% and the content of pyridinic-N increased from 18.1% to 22.6%. The higher content of pyrrolic-N at the edges could improve the charge mobility and electrocatalytic activity of PNDC. The P doping in PNDC was also confirmed by XPS with a typical P-C bond centered at 132.9 eV and P-O bond centered at 133.8 eV.⁵⁵ As shown in Supplementary Fig. 7, both PNDC and NDC have the typical carbon D band and G band. The D band located at 1350 cm^{-1} could be attributed to disordered carbon atoms, while the G band observed at 1580 cm^{-1} can be ascribed to sp^2 -hybridized graphitic carbon atoms. In addition, the I_D/I_G intensity ratio slightly decreases from NDC (1.19) to PNDC (1.14), indicating that the defects are reduced after introducing P atoms.

Electrochemical properties investigations of PNDC and NDC

In order to investigate the electrochemical properties of the as-prepared materials, Na-O₂ batteries were tested using PNDC and NDC as air cathodes. The specific capacities were calculated based on the mass of active materials in the cathodes. Cyclic voltammetry curves of the two electrodes were measured to demonstrate their catalytic activities. As shown in Fig. 2a, the PNDC has higher anodic and cathodic peaks current densities and lower overpotential than the NDC electrode, indicating that the PNDC exhibits superior catalytic activity. In addition, the PNDC electrode also has better conductivity compared with the NDC electrode, as demonstrated by the Nyquist plots in Supplementary Fig. 8. The full galvanostatic discharge/charge plot in the voltage range of 1.5-4.0 V at room temperature at current density of 200 mA g^{-1} is shown in Supplementary Fig. 9. The Na-O₂ batteries with the PNDC cathode achieved a discharge capacity of 6216 mAh g^{-1} , which is much higher than that of the battery with the NDC electrode (4975 mAh g^{-1}). Based on the total weight of air cathode, PNDC cathode could deliver a high energy density of 440.57 Wh kg^{-1} . Compared with the NDC electrode, the PNDC electrode also exhibits much lower overpotential and higher coulombic efficiency. Figure 2b presents the discharge/charge curves of Na-O₂ batteries with PNDC and NDC cathodes with a cut-off capacity of 2000 mAh g^{-1} at a current density of 400 mA g^{-1} . The charge plateaus at 2.45 V corresponding to the decomposition of NaO₂ discharge products.⁵⁶ It is obvious that the PNDC air cathode has much higher round trip efficiency compared with NDC air cathode, indicating PNDC exhibits better OER performance than NDC. In addition, the PNDC also demonstrates outstanding rate capability. When the current densities were increased from 100 to 200 or even 400 mA g^{-1} , as shown in Fig. 2c-d and Supplementary Fig. 10, the PNDC still exhibited a low

overpotential (0.36 V). Meanwhile, the recharge capacities of the PNDC air cathodes also increased from 593 to 797 mAh g⁻¹, which is consistent with other reports.^{36, 57, 58, 59} In contrast, the NDC air cathode only delivered a recharge capacity of 389 mAh g⁻¹ even at the current density of 400 mA g⁻¹. The excellent electrochemical performance and rate capability of the PNDC air cathode are primarily attributable to its high catalytic activity and excellent stabilizing ability for the NaO₂ discharge products (would be discussed later). Figure 2e-g and Supplementary Fig. 10b evaluate the cyclability of PNDC and NDC electrodes at a current density of 200 mA g⁻¹ with a fixed specific capacity of 1000 mA h g⁻¹. The NDC electrode demonstrated unsatisfactory electrochemical performance when used as an air electrode in the Na-O₂ batteries. Compared with NDC, the discharge and charge capacities of the PNDC are still as high as 1000 and 845 mAh g⁻¹ after 120 cycles, respectively, indicating the excellent energy efficiency of the Na-O₂ batteries based on PNDC air cathode. The PNDC air cathodes thus exhibit better cycling performance with low overpotential, which is one of the best reported air cathodes for the Na-O₂ batteries (Fig. 2f). In comparison, the NDC electrode only exhibited a recharge capacity of 216 mAh g⁻¹ for the first cycle, while its discharge capacity decreased to 878 mAh g⁻¹ for 19 cycles. The improved cycling performance of the PNDC air electrode is primarily attributable to its excellent catalytic activity and outstanding stability during a long cycling period.

Investigation of reaction mechanism

In order to gain an in depth understanding of the reaction mechanism on the PNDC and NDC electrodes, in-situ synchrotron XRD, ex-situ XRD and SEM were conducted on these electrodes. As shown in Fig. 3a-b, the crystal evaluation of PNDC electrode air cathode was investigated with in-situ synchrotron, using the Powder Diffraction Beamline with $\lambda = 0.7749 \text{ \AA}$ (Australia Synchrotron). In-situ synchrotron XRD is a crucial tool to analyze the crystallographic information of materials and it will help to determine the electrochemical reaction mechanism of Na-O₂ batteries. During the initial discharge process, there is a new diffraction peak developed at 23.15°, which could be indexed to the (220) plane of NaO₂ with d-spacing of 1.93 Å (JCPDF no. 01-089-5951). Then that peak disappeared during the initial recharge process, indicating the reversible formation and decomposition of NaO₂ discharge products, which is consistent with the ex-situ XRD results (Fig. 3c-d, and Supplementary Fig. 11). With an eye on the stabilize ability of different air cathode materials for NaO₂ discharge products, the crystal structure evaluation of discharge products was also investigated by using ex-situ XRD. For the discharged PNDC air cathode, the diffraction peaks of NaO₂ discharge products could be well preserved after 8 hours rested without any obvious difference, demonstrating the excellent stabilize ability of PNDC air cathode towards the NaO₂ discharge products. For the discharged NDC air cathodes, however, the intensities of NaO₂ discharged products diffraction peaks are significantly decreased associated with the emerging of diffraction peaks of Na₂O₂·2H₂O (JCPDF no. 00-015-0064) after 2 hours rested. With the increase of rest times to 4 and 8 hours, the diffraction peaks of NaO₂ finally disappeared and only Na₂O₂·2H₂O could be detected, implying all the NaO₂ discharge products were transformed into Na₂O₂·2H₂O on the NDC air cathodes. As the water content in the electrolyte was less than 5 ppm, this phenomenon could be assigned to the

spontaneous dissolution and ionization of NaO_2 discharge products associated with the decomposition of the electrolyte.³⁶ With the formation of $\text{Na}_2\text{O}_2 \cdot 2\text{H}_2\text{O}$ side products, the electrochemical performance of Na- O_2 batteries would be significantly diminished with increased overpotential, decreased coulombic efficiency, and declined cycling stability. As the PNDC and NDC air cathodes have quite similar morphology and structure, their diverse stabilize abilities towards NaO_2 discharge products on different air cathodes could be attributed to the different absorption energy for NaO_2 driven by their different elements doping. As shown in Supplementary Fig. 12 and Supplementary Fig. 13, NaO_2 nanoparticles discharge products within the size range of 150–200 nm were gradually formed and deposited on the surface of PNDC and NDC electrodes during discharging process. The NaO_2 nanoparticles discharge products would be decomposed and totally disappeared after recharging to 3.0 V. Supplementary Fig. 12f illustrated the ORR pathway of electrochemical formation of the NaO_2 nanoparticles discharge products. O_2 first adsorbs on the surface of the electrode and then undergoes a one-electron electrochemical reduction to form NaO_2 . Finally, the NaO_2 would subsequently precipitate from the solution and deposit on the electrodes to form NaO_2 nanoparticles.

To confirm our hypothesis about the outstanding stabilize ability and excellent electrochemical activity of PNDC, DFT calculations are carried out to investigate the absorption energy of NaO_2 discharge products and OER reaction processes. As can be found in Supplementary Table 1, PNDC has much stronger adsorption energy (-2.85 eV) for NaO_2 than that of NDC (-1.80 eV). The strong adsorption energy could inhibit the generation of liberated O_2^- from the dissolution of NaO_2 , which is a strong reagent and could react with the electrolyte to form $\text{Na}_2\text{O}_2 \cdot 2\text{H}_2\text{O}$ side product.³⁶ Therefore, the strong adsorption energy of the PNDC for NaO_2 could excellently stabilize the NaO_2 discharge products and prevent its spontaneous dissolution and ionization to form $\text{Na}_2\text{O}_2 \cdot 2\text{H}_2\text{O}$. This ability would enhance the electrochemical performance of the PNDC air cathode through avoiding the formation of $\text{Na}_2\text{O}_2 \cdot 2\text{H}_2\text{O}$ side products. Moreover, OER reaction processes on the PNDC and NDC are shown in Fig. 4, in which five transition states were selected with a nudged elastic band (NEB) calculation. As shown in Fig. 4a, the first three steps are all a result of endothermic reactions and the following three steps are exothermic reactions. In the case of PNDC, only near-zero free uphill energies are required for the first three steps. The highest free energy required is 0.33 eV for the first step. In the case of NDC, however, much higher uphill energies are required for the first three steps. And the step 2 even needs to overcome a free energy barrier of 1.53 eV. Based on the above DFT calculations, the PNDC possesses high intrinsic electrocatalytic activity with less free energy compared to the NDC. As illustrated in Fig. 4b, the PNDC has excellent electrocatalytic activity to decompose the NaO_2 discharge products during the OER reaction process of Na- O_2 batteries. Moreover, it has stronger adsorption energy for NaO_2 to stabilize the discharge products of Na- O_2 batteries.

Discussion

In conclusion, the PNDC air cathode was synthesized and employed as electrocatalyst for the Na-O₂ batteries, which could facilitate the formation and stabilization of NaO₂ nanoparticles as discharge products with a quite low overpotential (0.36 V) and long cycling stability for 120 cycles. The excellent electrochemical performance of the PNDC electrodes could be attributed to its strong adsorption energy and outstanding electrocatalytic activity during recharging process. As confirmed by in-situ synchrotron XRD, ex situ XRD, and DFT calculations, the PNDC could effectively prevent the transform of NaO₂ discharge products to Na₂O₂·2H₂O side products and facilitate the decomposition of NaO₂ discharge products with its outstanding electrocatalytic activity during recharging process. In addition, this work could help us to achieve an in-depth understanding of the influence of electrocatalysts on the composition of discharge products and provide a new direction to design high performance electrocatalysts with favorable absorption energy and electrocatalytic activity for metal-oxygen/metal carbon dioxide batteries.

Methods

Synthesis of polypyrrole

Polypyrrole was fabricated by a previously reported method.⁶⁰ Generally, 81.8 mg methyl orange and 1350 mg FeCl₃ were dissolved in 100 mL deionized water. Then, 33.5 mg pyrrole monomer was added into the above solution. After stirring at room temperature for 24 h, the polypyrrole was washed with ethanol and deionized water several times.

Synthesis of phosphorus and nitrogen dual-doped carbon

Polypyrrole was placed on a porcelain boat in a tube furnace under argon atmosphere. Another porcelain boat with NaH₂PO₂ was put on the upstream side. Then, the sample was annealed at 300 °C for 2 h with a heating rate of 5 °C min⁻¹. Finally, the sample was washed with ethanol and deionized water several times after cooling down to room temperature. To synthesize nitrogen doped carbon, the polypyrrole alone was put into the tube furnace with the same annealing conditions.

Materials Characterization

Powder XRD on a GBC MMA diffractometer with Cu K α radiation was utilized to study the crystalline structures of the samples. Raman spectra were investigated with a JOBIN YVON HR800 Confocal system. A Phoibos 100 Analyzer XPS with Al K α X-rays was used to determine the surface chemical states of the samples. A JSM-7500FA scanning electron microscope and JEM-ARM200F transmission electron microscope were utilized to measure the structures and morphologies of the materials. In-situ synchrotron XRD measurements were conducted at the Powder diffraction beamline (Australia Synchrotron) using CR2032-type coin cells with holes in the cathode part in dry oxygen atmosphere with our designed facility. A 4 mm hole sealed with the Kapton film was punched in the anode part, which could allow the X-ray beams penetrate the cell.

Electrochemical Measurements of Na-O₂ Batteries: The electrochemical properties were measured employing CR2032-type coin cells with holes in the cathode part. To prepare the oxygen cathodes, the active materials and poly(tetrafluoroethylene) solution were mixed in the ratio of 90:10 in isopropyl alcohol as catalyst slurry. The slurry was then pasted onto carbon paper and dried in a vacuum oven at 120 °C for 12 h. The typical loading of cathode active materials was 0.3 mg cm⁻². Tetraethylene glycol dimethyl ether (TEGDME) solvent was purified by rotary evaporation and stored with 4 Å activated molecular sieves for two weeks before use. Sodium trifluoromethanesulfonate (sodium triflate, NaSO₃CF₃) was dried at 120 °C for 24 h under vacuum. The electrolyte, consisting of 0.5 m sodium triflate in TEGDME, was prepared in an argon-filled glovebox. The water content in the electrolyte was less than 5 ppm as measured by Karl-Fischer titration. The cells were assembled in an argon-filled MBRAUN glove box (H₂O level < 0.1 ppm and O₂ level < 0.1 ppm). A piece of sodium cut from a sodium cube served as the anode, and glass microfiber was used as the separator. All the measurements were carried out on Neware battery testers at room temperature in dry oxygen atmosphere with our designed facility. Cyclic voltammetry was measured on a Biologic VMP-3 electrochemical workstation with a scan rate of 0.1 mV/s. Electrochemical impedance spectroscopy curves were collected in the frequency range of 100 kHz to 0.1 Hz.

Computational Method

In this study, the density functional theory (DFT) calculation was implemented using the Vienna Ab-Initio Simulation Package.⁶¹ The electron-ion interaction was described by projector augmented-wave (PAW) pseudopotentials. For the exchange and correlation functionals, the Perdew-Burke-Ernzerhof (PBE) version of the generalized gradient approximation (GGA) exchange-correlation was applied.^{62, 63} In the DFT calculation, 450 eV as the cut off kinetic energy was used for the wave functions expansion. In order to avoid the interactions between each carbon layers, a vacuum width of 15 Å was applied. In the brillouin zone integration on the grid with 3 × 3 × 1 and 5 × 5 × 1 were respectively used during the geometry optimization. To better understand the catalytic ability of NaO₂ on the surface of different PNDC, the climbing image nudged elastic band (CI-NEB) method⁶⁴ was used to simulate the possibility of degradation of NaO₂. In addition, five images were inserted between the initial and final configurations in the transition state search began with a NEB calculation. And the corrected adsorption energy of NaO₂ (ΔE_{ads}) was defined as

$$\Delta E_{ads} = E_{total} - E_{host} - E_{guest}$$

Where E_{total} is the total energy of PNDC and NDC surface adsorbed with the NaO₂, E_{host} is the total energy of PNDC and NDC, and E_{guest} is the total energy of NaO₂.

Declarations

Data Availability

Data supporting the findings of this study are available from the authors on reasonable request. See author contributions for specific data sets.

Competing interests

The authors declare no competing interests.

Contributions

H.G., S.C., and J.W. designed and conducted the experimental work. Z.Z and Z.H. performed the Raman and XPS measurements. Z.H. and F.G. helped with analyzing the electrochemical data. H.G, Z.Z., and Q.G. performed synchrotron X-ray diffraction measurements. H.G., C.S., S.C., K.K., H.L, and J.W. analyzed the data and wrote the manuscript.

Acknowledgement

Financial support received from the Australian Research Council (ARC) Discovery Project (DP180101453) is greatly appreciated. The authors also are grateful for the use of the facilities in the UOW Electron Microscopy Center and the Powder Diffraction Beamline at the Australia Synchrotron. Many thanks to Dr. Tania Silver for critically reading the manuscript.

Author information

Affiliations

Institute for Superconducting and Electronic Materials, University of Wollongong, Innovation Campus, Squires Way, North Wollongong, NSW, 2522, Australia

Haipeng Guo, Zhi Zheng, Chaozhu Shu, Zhe Hu, Florian Gebert, Konstantin Konstantinov, Shu-Lei Chou, Hua-Kun Liu & Jia-Zhao Wang

College of Materials and Chemistry & Chemical Engineering, Chengdu University of Technology, 1#, Dongsanlu, Erxianqiao, Chengdu 610059, Sichuan, PR China

Chaozhu Shu

Australian Synchrotron, 800 Blackburn Road, Clayton, VIC, 3168, Australia

Qin-Fen Gu

References

1. Zhang, P., Zhao Y., Zhang X. Functional and stability orientation synthesis of materials and structures in aprotic Li-O₂ batteries. *Chem. Soc. Rev.* **47**, 2921–3004 (2018).
2. Ma, L., *et al.* Fundamental Understanding and Material Challenges in Rechargeable Nonaqueous Li-O₂ Batteries: Recent Progress and Perspective. *Adv. Energy Mater.* **8**, 1800348 (2018).
3. Yang, S. X., He P., Zhou H. S. Research progresses on materials and electrode design towards key challenges of Li-air batteries. *Energy Storage Materials* **13**, 29–48 (2018).
4. Wang, J., Li Y., Sun X. Challenges and opportunities of nanostructured materials for aprotic rechargeable lithium–air batteries. *Nano Energy* **2**, 443–467 (2013).
5. Guo, H., *et al.* Review of Electrolytes in Nonaqueous Lithium-Oxygen Batteries. *Adv. Sustainable Syst.* **2**, 1700183 (2018).
6. Luo, W. B., Gao X. W., Chou S. L., Wang J. Z., Liu H. K. Porous AgPd-Pd Composite Nanotubes as Highly Efficient Electrocatalysts for Lithium-Oxygen Batteries. *Adv. Mater.* **27**, 6862–6869 (2015).
7. Peng, Z., Freunberger S. A., Chen Y., Bruce P. G. A reversible and higher-rate Li-O₂ battery. *Science* **337**, 563–566 (2012).
8. Chen, Y., Gao X., Johnson L. R., Bruce P. G. Kinetics of lithium peroxide oxidation by redox mediators and consequences for the lithium-oxygen cell. *Nat. Commun.* **9**, 767 (2018).
9. Song, K., Agyeman D. A., Park M., Yang J., Kang Y. M. High-Energy-Density Metal-Oxygen Batteries: Lithium-Oxygen Batteries vs Sodium-Oxygen Batteries. *Adv. Mater.* **29**, (2017).
10. Peng, Z., *et al.* Oxygen reactions in a non-aqueous Li⁺ electrolyte. *Angew. Chem., Int. Ed.* **50**, 6351–6355 (2011).
11. Luo, W. B., Pham T. V., Guo H. P., Liu H. K., Dou S. X. Three-Dimensional Array of TiN@Pt₃Cu Nanowires as an Efficient Porous Electrode for the Lithium-Oxygen Battery. *ACS Nano* **11**, 1747–1754 (2017).
12. Hartmann, P., *et al.* A rechargeable room-temperature sodium superoxide (NaO₂) battery. *Nat. Mater.* **12**, 228–232 (2013).
13. Yadegari, H., Sun Q., Sun X. Sodium-Oxygen Batteries: A Comparative Review from Chemical and Electrochemical Fundamentals to Future Perspective. *Adv. Mater.* **28**, 7065–7093 (2016).
14. Wu, S. C., *et al.* Tailoring Sodium Anodes for Stable Sodium-Oxygen Batteries. *Adv. Funct. Mater.* **28**, 1706374 (2018).
15. Aldous, I. M., Hardwick L. J. Solvent-Mediated Control of the Electrochemical Discharge Products of Non-Aqueous Sodium-Oxygen Electrochemistry. *Angew. Chem., Int. Ed.* **55**, 8254–8257 (2016).
16. Xia, C., Black R., Fernandes R., Adams B., Nazar L. F. The critical role of phase-transfer catalysis in aprotic sodium oxygen batteries. *Nat. Chem.* **7**, 496–501 (2015).
17. Zhang, S. P., *et al.* Graphene nanosheets loaded with Pt nanoparticles with enhanced electrochemical performance for sodium-oxygen batteries. *J. Mater. Chem. A* **3**, 2568–2571 (2015).
18. Yadegari, H., *et al.* On rechargeability and reaction kinetics of sodium–air batteries. *Energy Environ. Sci.* **7**, 3747–3757 (2014).

19. Shang, M., Liu Y., Xia J., Zhang S., Yang J. Synthesis and characterization of MnCo_2O_4 microspheres based air electrode for rechargeable sodium-air batteries. *Ceramics International* **43**, 3218–3223 (2017).
20. Ma, J.-L., Meng F.-L., Xu D., Zhang X.-B. Co-embedded N-doped carbon fibers as highly efficient and binder-free cathode for $\text{Na}-\text{O}_2$ batteries. *Energy Storage Materials* **6**, 1–8 (2017).
21. Liu, Y., *et al.* Vertically self-standing $\text{C@NiCo}_2\text{O}_4$ nanoneedle arrays as effective binder-free cathodes for rechargeable $\text{Na}-\text{O}_2$ batteries. *J. Alloys Compd.* **772**, 693–702 (2019).
22. Liu, W.-M., Yin W.-W., Ding F., Sang L., Fu Z.-W. NiCo_2O_4 nanosheets supported on Ni foam for rechargeable nonaqueous sodium–air batteries. *Electrochem. Commun.* **45**, 87–90 (2014).
23. Zhang, S., *et al.* Controlling uniform deposition of discharge products at the nanoscale for rechargeable $\text{Na}-\text{O}_2$ batteries. *J. Mater. Chem. A* **4**, 7238–7244 (2016).
24. Kwak, W.-J., *et al.* Nanoconfinement of low-conductivity products in rechargeable sodium–air batteries. *Nano Energy* **12**, 123–130 (2015).
25. Hu, Y. X., *et al.* Porous perovskite calcium-manganese oxide microspheres as an efficient catalyst for rechargeable sodium-oxygen batteries. *J. Mater. Chem. A* **3**, 3320–3324 (2015).
26. Li, Y., *et al.* Superior catalytic activity of nitrogen-doped graphene cathodes for high energy capacity sodium-air batteries. *Chem. Commun.* **49**, 11731–11733 (2013).
27. Liu, W., Sun Q., Yang Y., Xie J. Y., Fu Z. W. An enhanced electrochemical performance of a sodium-air battery with graphene nanosheets as air electrode catalysts. *Chem. Commun.* **49**, 1951–1953 (2013).
28. Kim, J., Lim H. D., Gwon H., Kang K. Sodium-oxygen batteries with alkyl-carbonate and ether based electrolytes. *Phys. Chem. Chem. Phys.* **15**, 3623–3629 (2013).
29. Jian, Z., *et al.* High capacity $\text{Na}-\text{O}_2$ batteries with carbon nanotube paper as binder-free air cathode. *J. Power Sources* **251**, 466–469 (2014).
30. Liu, C., *et al.* Growth of NaO_2 in Highly Efficient $\text{Na}-\text{O}_2$ Batteries Revealed by Synchrotron In Operando X-ray Diffraction. *ACS Energy Lett.* **2**, 2440–2444 (2017).
31. Sun, Q., *et al.* Visualizing the Oxidation Mechanism and Morphological Evolution of the Cubic-Shaped Superoxide Discharge Product in $\text{Na}-\text{Air}$ Batteries. *Adv. Funct. Mater.* **29**, 1808332 (2019).
32. Wu, F., *et al.* Micrometer-Sized RuO_2 Catalysts Contributing to Formation of Amorphous Na -Deficient Sodium Peroxide in $\text{Na}-\text{O}_2$ Batteries. *Adv. Funct. Mater.* **27**, 1700632 (2017).
33. He, M., *et al.* Concentrated Electrolyte for the Sodium-Oxygen Battery: Solvation Structure and Improved Cycle Life. *Angew. Chem., Int. Ed.* **55**, 15310–15314 (2016).
34. Elia, G. A., Hasa I., Hassoun J. Characterization of a reversible, low-polarization sodium-oxygen battery. *Electrochim. Acta* **191**, 516–520 (2016).
35. Sun, Q., *et al.* Atomic Layer Deposited Non-Noble Metal Oxide Catalyst for Sodium–Air Batteries: Tuning the Morphologies and Compositions of Discharge Product. *Adv. Funct. Mater.* **27**, 1606662

- (2017).
36. Kim, J., *et al.* Dissolution and ionization of sodium superoxide in sodium-oxygen batteries. *Nat. Commun.* **7**, 10670 (2016).
 37. Landa-Medrano, I., *et al.* New Insights into the Instability of Discharge Products in Na–O₂ Batteries. *ACS Applied Materials & Interfaces* **8**, 20120–20127 (2016).
 38. Yadegari, H., *et al.* Revealing the Chemical Mechanism of NaO₂ Decomposition by In Situ Raman Imaging. *Chem. Mater.* **30**, 5156–5160 (2018).
 39. Lau, S., Archer L. A. Batteries: Discharging the right product. *Nature Energy* **1**, 16019 (2016).
 40. Kang, S., Mo Y., Ong S. P., Ceder G. Nanoscale stabilization of sodium oxides: implications for Na-O₂ batteries. *Nano Lett.* **14**, 1016–1020 (2014).
 41. Park, H., *et al.* Highly Durable and Stable Sodium Superoxide in Concentrated Electrolytes for Sodium-Oxygen Batteries. *Adv. Energy Mater.* **8**, 1801760 (2018).
 42. Sheng, C., Yu F., Wu Y., Peng Z., Chen Y. Disproportionation of Sodium Superoxide in Metal–Air Batteries. *Angew. Chem., Int. Ed.* **57**, 9906–9910 (2018).
 43. Chen, S., Duan J., Jaroniec M., Qiao S. Z. Nitrogen and oxygen dual-doped carbon hydrogel film as a substrate-free electrode for highly efficient oxygen evolution reaction. *Adv. Mater.* **26**, 2925–2930 (2014).
 44. Zhao, S., Wang D. W., Amal R., Dai L. Carbon-Based Metal-Free Catalysts for Key Reactions Involved in Energy Conversion and Storage. *Adv. Mater.* **31**, e1801526 (2019).
 45. Wang, J., Zhong H. X., Wang Z. L., Meng F. L., Zhang X. B. Integrated Three-Dimensional Carbon Paper/Carbon Tubes/Cobalt-Sulfide Sheets as an Efficient Electrode for Overall Water Splitting. *ACS Nano* **10**, 2342–2348 (2016).
 46. Xia, L., *et al.* Graphene coated carbon felt as a high-performance electrode for all vanadium redox flow batteries. *Surf. Coat. Technol.* **358**, 153–158 (2019).
 47. Sun, B., *et al.* Hierarchical Porous Carbon Spheres for High-Performance Na-O₂ Batteries. *Adv. Mater.* **29**, 1606816 (2017).
 48. Liang, J., Jiao Y., Jaroniec M., Qiao S. Z. Sulfur and nitrogen dual-doped mesoporous graphene electrocatalyst for oxygen reduction with synergistically enhanced performance. *Angew. Chem., Int. Ed.* **51**, 11496–11500 (2012).
 49. Liang, J., Du X., Gibson C., Du X. W., Qiao S. Z. N-doped graphene natively grown on hierarchical ordered porous carbon for enhanced oxygen reduction. *Adv. Mater.* **25**, 6226–6231 (2013).
 50. Zheng, Y., Jiao Y., Ge L., Jaroniec M., Qiao S. Z. Two-step boron and nitrogen doping in graphene for enhanced synergistic catalysis. *Angew. Chem., Int. Ed.* **52**, 3110–3116 (2013).
 51. Jiao, Y., Zheng Y., Jaroniec M., Qiao S. Z. Origin of the electrocatalytic oxygen reduction activity of graphene-based catalysts: a roadmap to achieve the best performance. *J. Am. Chem. Soc.* **136**, 4394–4403 (2014).

52. Gong, K., Du F., Xia Z., Durstock M., Dai L. Nitrogen-doped carbon nanotube arrays with high electrocatalytic activity for oxygen reduction. *Science* **323**, 760–764 (2009).
53. Shu, C., Lin Y., Zhang B., Abd Hamid S. B., Su D. Mesoporous boron-doped onion-like carbon as long-life oxygen electrode for sodium–oxygen batteries. *J. Mater. Chem. A* **4**, 6610–6619 (2016).
54. Ma, J.-l., Zhang X.-b. Optimized nitrogen-doped carbon with a hierarchically porous structure as a highly efficient cathode for Na–O₂ batteries. *J. Mater. Chem. A* **4**, 10008–10013 (2016).
55. Li, K., *et al.* Nitrogen, phosphorus co-doped carbon cloth as self-standing electrode for lithium-iodine batteries. *Nano Res.* **12**, 549–555 (2018).
56. Schafzahl, L., *et al.* Singlet Oxygen during Cycling of the Aprotic Sodium-O₂ Battery. *Angew. Chem., Int. Ed.* **56**, 15728–15732 (2017).
57. Yadegari, H., *et al.* Three-Dimensional Nanostructured Air Electrode for Sodium-Oxygen Batteries: A Mechanism Study toward the Cyclability of the Cell. *Chem. Mater.* **27**, 3040–3047 (2015).
58. Wu, F., *et al.* Micrometer-Sized RuO₂ Catalysts Contributing to Formation of Amorphous Na-Deficient Sodium Peroxide in Na–O₂ Batteries. *Adv. Funct. Mater.* **27**, 1700632 (2017).
59. Sun, Q., *et al.* Visualizing the Oxidation Mechanism and Morphological Evolution of the Cubic-Shaped Superoxide Discharge Product in Na–Air Batteries. *Adv. Funct. Mater.* **0**, 1808332.
60. Li, M., Li W., Liu J., Yao J. Preparation and characterization of PPy with methyl orange as soft template. *J. Mater. Sci.: Mater. Electron.* **24**, 906–910 (2013).
61. Kresse, G., Joubert D. From ultrasoft pseudopotentials to the projector augmented-wave method. *Physical Review B* **59**, 1758–1775 (1999).
62. Perdew, J. P., Burke K., Ernzerhof M. Generalized Gradient Approximation Made Simple. *Physical Review Letters* **77**, 3865–3868 (1996).
63. Blöchl, P. E. Projector augmented-wave method. *Physical Review B* **50**, 17953–17979 (1994).
64. Henkelman, G., Uberuaga B. P., Jónsson H. A climbing image nudged elastic band method for finding saddle points and minimum energy paths. *The Journal of chemical physics* **113**, 9901–9904 (2000).

Figures

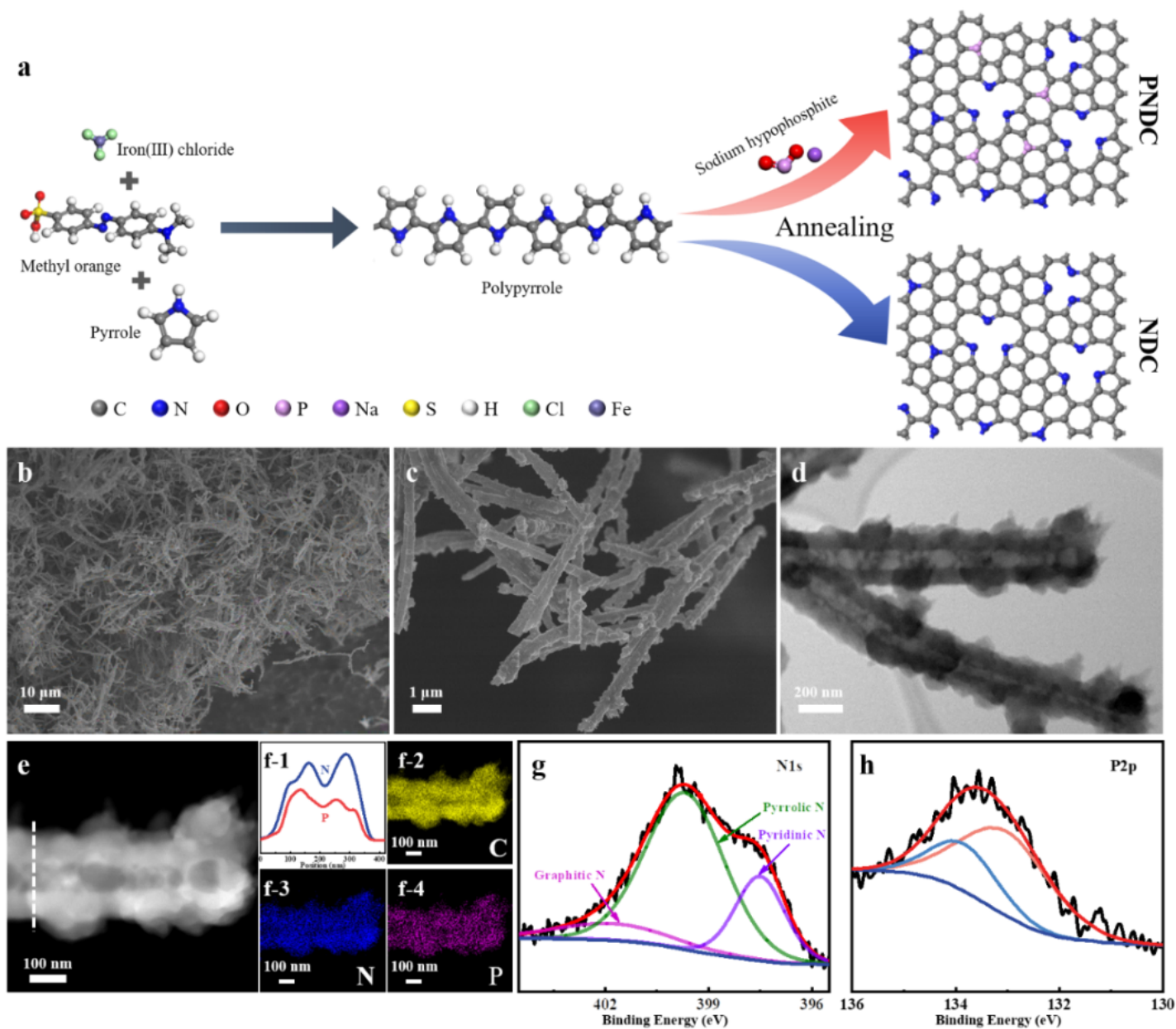


Figure 1

Structural characterization of the PNDC. (a) Schematic illustration of the preparation process for PNDC and NDC, in which the structures of PNDC and NDC are optimized with density function theory (DFT) calculation; (b) Low magnification SEM image of the PNDC; (c) high magnification SEM image of the PNDC; (d) STEM image of PNDC; (e) high-angle annular dark-field STEM image of an individual PNDC; (f) corresponding element mappings of various elements, (f-1) liner scan of P and N elements; (g) high resolution N 1s XPS spectrum, and (h) high resolution P 2p XPS spectrum of PNDC.

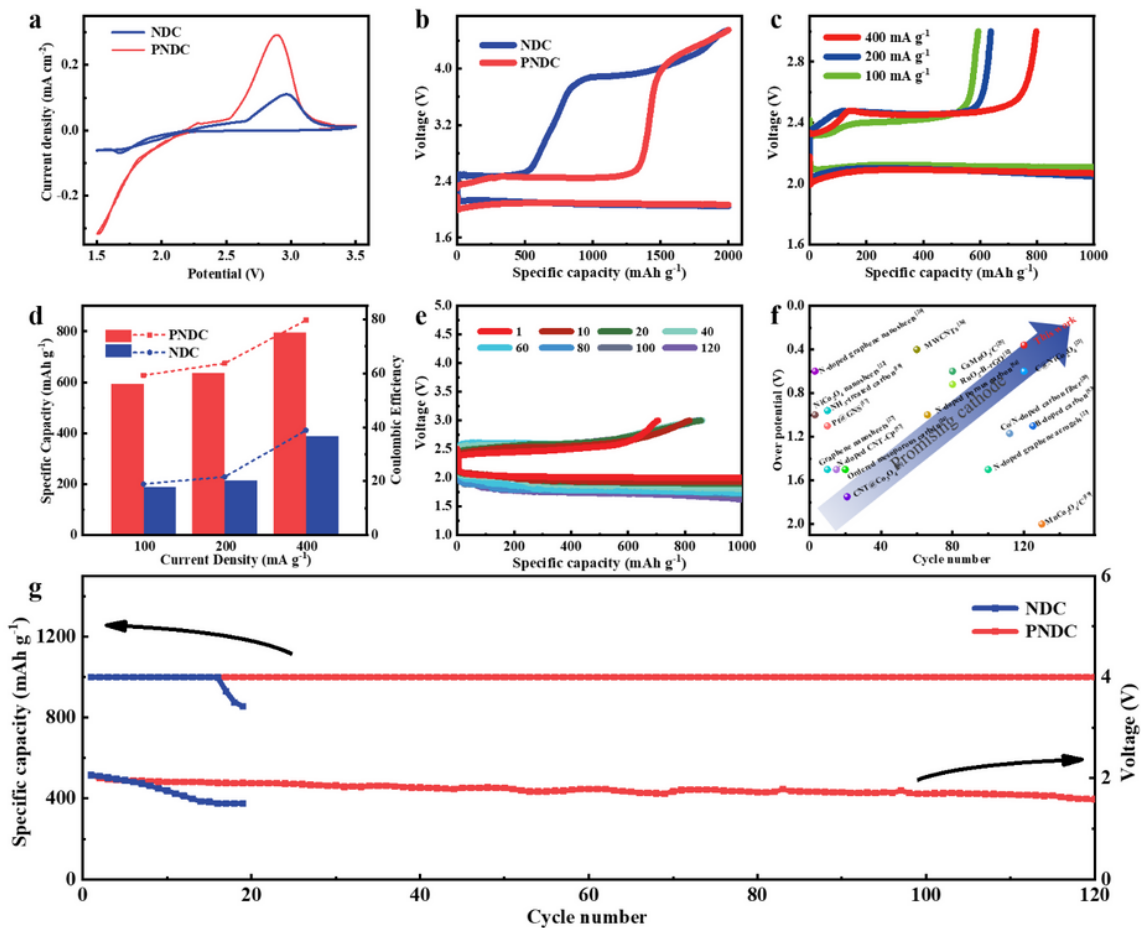


Figure 2

Electrochemical performance of the PNDC and NDC. (a) cyclic voltammetry curves of the PNDC and NDC; (b) comparison of the discharge/charge plots of the PNDC and NDC at a current density of 400 mA g⁻¹ with a cut-off specific capacity of 2000 mAh g⁻¹; (c) discharge/charge curves of the PNDC at different current densities; (d) comparison of recharge capacities of the PNDC and NDC at different current densities; (e) discharge/charge curves of the PNDC for selected cycles at a current density of 200 mA g⁻¹; (f) the electrochemical performance of PNDC and reported air cathodes for Na-O₂ batteries; (g) comparison of cycling performance of the PNDC and NDC electrodes at a current density of 200 mA g⁻¹.

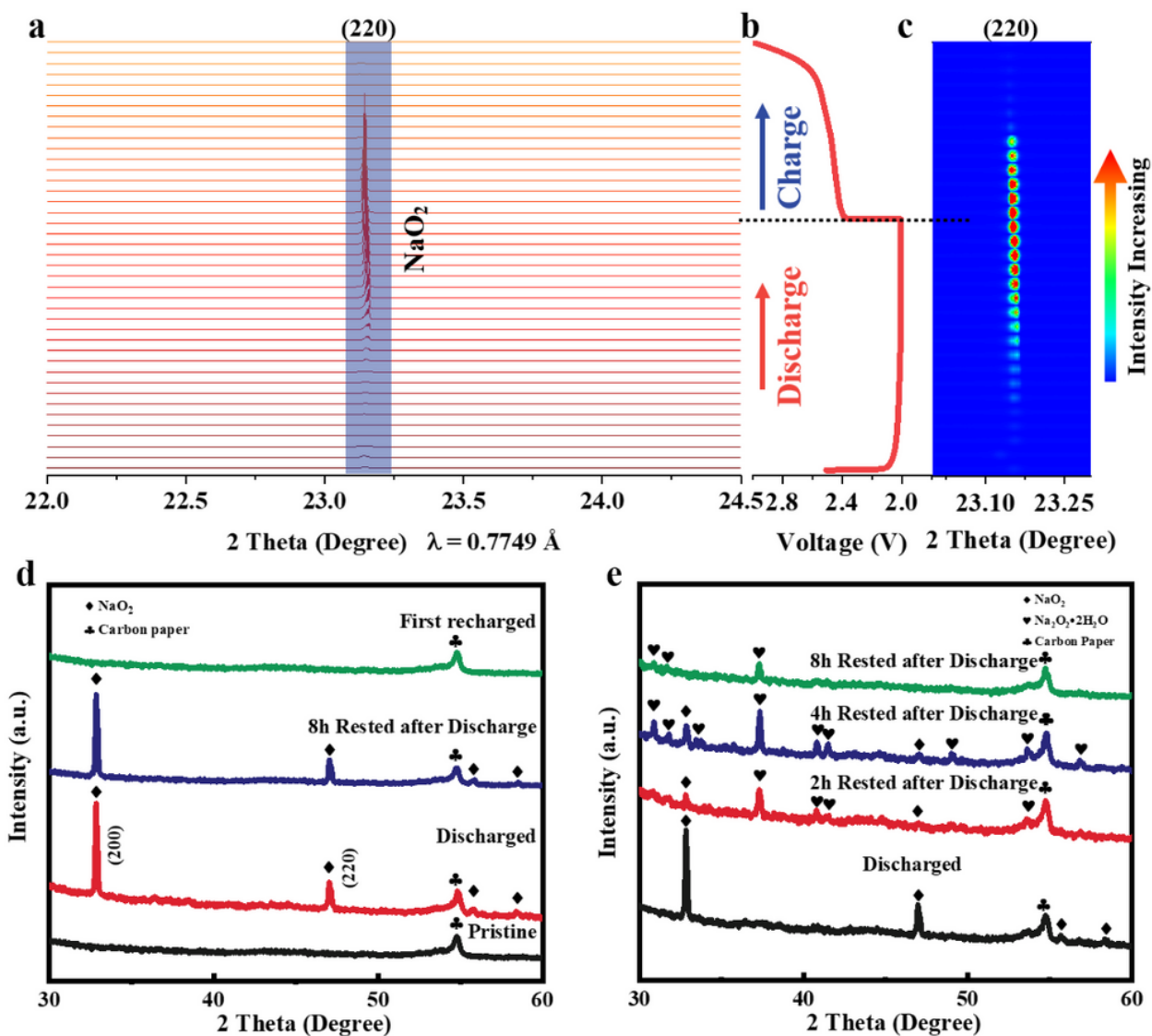


Figure 3

Analysis of the discharge products of Na-O₂ batteries. (a-b) in-situ synchrotron X-ray diffraction (XRD) pattern of the PNDC electrode with the initial galvanostatic discharge/charge curves at a current density of 200 mA g⁻¹; (c) XRD patterns of a pristine, a discharged, a recharged and a discharged with 8 hours rested PNDC electrodes; (d) XRD patterns of discharged NDC electrodes with rest times of 0, 2, 4, and 8 hours.

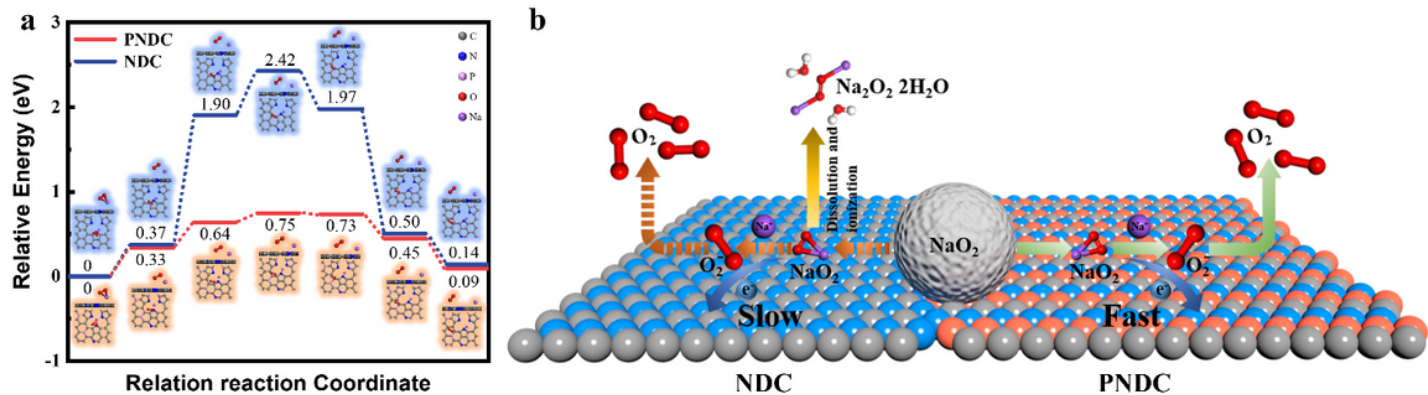


Figure 4

The oxygen evolution reaction (OER) of Na-O₂ batteries. (a) OER reaction processes on the PNDC (red shadow) and NDC (blue shadow) electrodes with side and top views, in which gray, blue, lavender, red, and purple atoms represent the carbon, nitrogen, phosphorous, oxygen, and sodium atoms, respectively; (b) schematic illustration of the OER reactions on PNDC and NDC electrodes.

Supplementary Files

This is a list of supplementary files associated with this preprint. Click to download.

- [SupplementaryInformation.docx](#)